Available online at www.sciencedirect.com
ScienceDirect
Journal of the European Ceramic Society 30 (2010) 1585–1597
www.elsevier.com/locate/jeurceramsoc

# Modeling thermal shock damage in refractory materials via direct numerical simulation (DNS)

I. Özdemir [a,b], W.A.M. Brekelmans [a], M.G.D. Geers [a,*]

[a] Department of Mechanical Engineering, Eindhoven University of Technology, P.O. Box 513, 5600 MB Eindhoven, The Netherlands
[b] Department of Manufacturing Engineering, Atılım University, Kızılcaşar Mah. 06836 İncek, Ankara, Turkey

Received 6 August 2009; received in revised form 23 November 2009; accepted 18 December 2009
Available online 27 January 2010

**Abstract**

In this paper, a computational investigation on thermo-mechanically induced damage in refractory materials resulting from severe thermal shock conditions is presented. On the basis of an idealized two-phase material system, molten aluminium thermal shock tests[1] are computationally modeled by means of direct numerical simulations (DNS). The interfacial and bulk damage evolution within the material are described by thermo-mechanical cohesive zones and continuum damage mechanics (CDM), respectively. Reported experimental results[1] are used to identify the parameters of the model. Furthermore, a parametric study is carried out to investigate the relative significance of various microstructure parameters in the context of thermal shock response.


*Keywords:* Thermal shock; Thermo-mechanical damage; DNS model; Thermo-mechanical cohesive zones; Heterogeneous materials

## 1. Introduction

In metal production plants, molten metal is transported and processed by means of structures made of high temperature resistant (refractory) materials. Under operation conditions, these structures are exposed to rapid temperature changes (thermal shock) and temperature change cycles, mainly due to contact with molten metal. Refractories with a high alumina ($Al_2O_3$) content and relatively large grained ceramics are used for the production of such structures. Making use of raw base materials in the production of these ceramics, the resulting microstructures are far from homogeneous.

When a heterogeneous material system experiences a temperature change, a stress field develops depending on the boundary conditions, the coefficient of thermal expansion (CTE) mismatch between the phases and the uniformity/non-uniformity of the temperature change within the domain of interest. To illustrate the essential mechanisms of the internal stress development, a representative two-phase material system of isotropic phases (both mechanically and thermally) is considered as shown in Fig. 1. In case of identical CTE's, a uniform temperature change within the body in combination with the given boundary conditions would lead to a stress free expansion or contraction. If a difference between the CTE's exists, under the same loading and boundary conditions, a self-equilibrated internal stress profile develops due to the mechanical strains resulting from non-uniform thermal expansion/contraction. Similarly, a non-uniform temperature change, e.g. occurrence of a temperature gradient, under certain external constraints, leads to internal stresses even in the case of matching CTE's. Therefore for common engineering materials and loading conditions, there are two mechanisms which lead to internal stresses. The first mechanism is associated with the CTE mismatch of the phases and the second mechanism is related to gradients in the resulting temperature profile which lead to non-uniform expansion or contraction. In this simple reasoning, it is implicitly assumed that the interface remains mechanically intact and acts as a perfect heat conductor. However, in real material systems, in general, the interfaces degrade mechanically after a certain threshold and consequently lose their ability to transmit stresses and to act as a perfect conductor. Therefore, when the thermal loading conditions reach significant levels, the initiation and propagation of material failure is dictated by the collective behaviour of the interfaces, individual phases, and the contrast in their

* Corresponding author. Tel.: +31 40 247 5076; fax: +31 40 244 7355.
*E-mail address:* M.G.D.Geers@tue.nl (M.G.D. Geers).

0955-2219/$ – see front matter © 2009 Elsevier Ltd. All rights reserved.
doi:10.1016/j.jeurceramsoc.2009.12.014

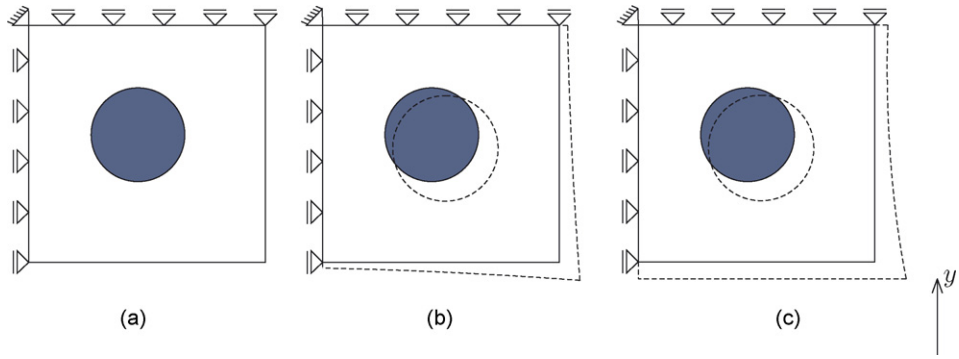


Fig. 1. Two-phase material system with different CTE's, (a) initial configuration, (b) uniform temperature change, (c) temperature gradient in $y$ direction (dashed lines correspond to the deformed shape).

mechanical and thermo-physical properties and fracture characteristics. For example, the average grain size dependency of residual strength observed in quenching tests on fine grained technical ceramics,[2–4] illustrates the microstructure–property relation under thermal shock conditions. The micromechanical origin of cracking in fine grained material systems upon temperature change has been investigated by relatively simple micromechanical models (semi-) analytically in Refs. 5–7. The characteristics of the solutions, e.g. stress singularities, were particularly useful to understand the significant role of grain size and to identify the potential sites of crack nucleation. Computational models have been used to investigate more complex geometries and different boundary conditions at the microlevel often relying on the concept of a representative volume element (RVE) and extracting macroscopic elastic properties.[8]

Approaching the problem from the macroscale, to enhance the understanding and modeling of thermo-mechanically induced damage, such as failure of refractory linings[9] and concrete failure under high temperatures,[10,11] predictive computational tools within the framework of continuum damage mechanics, have been developed. In such approaches, the heterogeneous microstructure is replaced by an equivalent 'homogeneous' material, which inevitably implies the loss of information associated with the heterogeneous nature of the microstructure. In some of these models, the local mechanisms, e.g. stresses due to a CTE mismatch, are smeared out by some extra terms in damage evolution laws in a phenomenological way, see Ref. 12. These approaches are computationally feasible tools for damage analysis of engineering structures but rather limited for the investigation of fundamental mechanisms determining the behaviour at the level of the microstructure.

Multi-scale computational models incorporating fine-scale physical mechanisms in their coarse-scale constitutive response are an accurate and feasible alternative for the analysis of engineering structures, see Ref. 13. However, the capabilities of such models heavily depend on the proper characterization of microscale material parameters. Direct measurement of physical properties at the scale of individual phases and interfaces, e.g. strength of an interface, is still a challenging task for experimentalists. Therefore, direct numerical simulations (DNS) within an inverse analysis framework constitute an alternative to determine these parameters, at least the correct order of magnitude, which can be a reliable data base for a multi-scale model.

To investigate the influence of microstructural parameters and to improve the understanding of material response under thermal loading conditions, thermal shock experiments are reproduced in a computational setting through fully resolved direct numerical simulation (DNS) models.

In the next section, the composition of the material microstructure is presented. Then, the experimental characterization and conducted experiments are summarized. Thereafter, the construction of the DNS model, the constitutive modeling of each phase and the solution procedure are outlined. Parameters of the model are determined on the basis of an equivalent static procedure, which is detailed in Section 4.5. Then, the focus is shifted on the influence of different material parameters, which is particularly relevant for the industry that processes these refractories. The paper is closed by the summary and conclusions.

## 2. Material microstructure

The initial chemical composition of the considered batch with a certain grading of particles is given in Table 1. The mixture is first mechanically pressed in a mould, resulting in a 'green product' and then sintered at 1900–2000 ° C to achieve a certain coherence and strength.

During the sintering process (phase), fine $SiO_2$ (approximately 0.2 μm) and $Al_2O_3$ particles react and result in a composite of mullite ($3Al_2O_32SiO_2$) which is by weight 71.8% $Al_2O_3$ and 28.2% $SiO_2$. Accordingly, the resulting product consists of 35.5% mullite with a very fine microstructure and 64.5% $Al_2O_3$ of various particle sizes. However, the reaction of $SiO_2$

Table 1
Initial chemical composition and final volume fractions.

| | |
|---|---|
| Chemical composition (relative weight of components) | |
| $Al_2O_3$ | 90.9% |
| $SiO_2$ | 8.8% |
| $Na_2O$ | 0.2% |
| Volumetric composition (volume percentages) | |
| Alumina | 59% |
| Mullite | 41% |

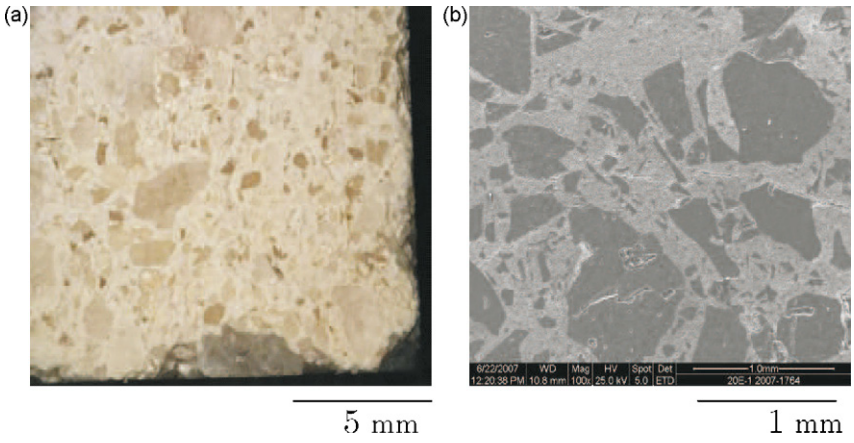


Fig. 2. Microstructure of the material: (a) light microscope image and (b) SEM image.

and $Al_2O_3$ is never fully complete and additionally an amorphous glass phase is formed consisting mainly of $Al_2O_3$, $SiO_2$ and impurities. In the following sections, the presence of this glass phase is neglected. Based on the measurements given in Ref. 14, the difference between the theoretical and measured density reveals that there exists a porosity of approximately 14%. Furthermore, it can be safely assumed that relatively large $Al_2O_3$ particles (particles of 3 and 0.875 mm, respectively) are free of any porosity. Representative images of the resulting microstructure is given in Fig. 2.

## 3. Experimental characterization of thermal shock response

Experimental investigations dealing with the thermal shock response of refractory materials are extensively reported in the literature, see Ref. 1 and the references cited therein. Typically, down-quenching experiments have been conducted by using different quenching mediums ranging from water to molten salt. For up-quenching, burners, molten metals and other techniques and devices have been utilized. Due to difficulties associated with the determination of the heat transfer conditions, these methods are not really suitable to adequately quantify the thermal shock response of different material systems.

Motivated by the shortcomings of the existing methods, mainly in realizing reproducible heat transfer conditions, in Ref. 1 refractory specimens were subjected repeatedly to surface contact with molten aluminium followed by passively cooling of the samples in ambient air. By measuring the transit time of longitudinal ultrasonic waves at various locations on the samples, the local damage is characterized in terms of reduction in the dynamic Young's modulus. The use of transit time measurement techniques to determine the damage in refractory materials with coarse grains is validated by independent experiments, see Ref. 1. The test set-up, the so-called 'molten aluminium thermal shock test' is schematically shown in Fig. 3. An equivalent computational testing procedure is developed starting with a DNS model of the experiment as presented in the next section.

## 4. Direct numerical simulation (DNS) of thermal shock experiments

As shown in Fig. 2, the resulting microstructure is composed of two distinguishable phases at a mm scale. Relatively large grains are identifiable, which can be assumed to be embedded in a compound of fine grains that constitute a rather monolithic continuous phase, i.e. the matrix. Therefore the microstructure is idealized as a two-phase composite with large, non-interacting grains of two different sizes (3 and 0.875 mm, respectively),

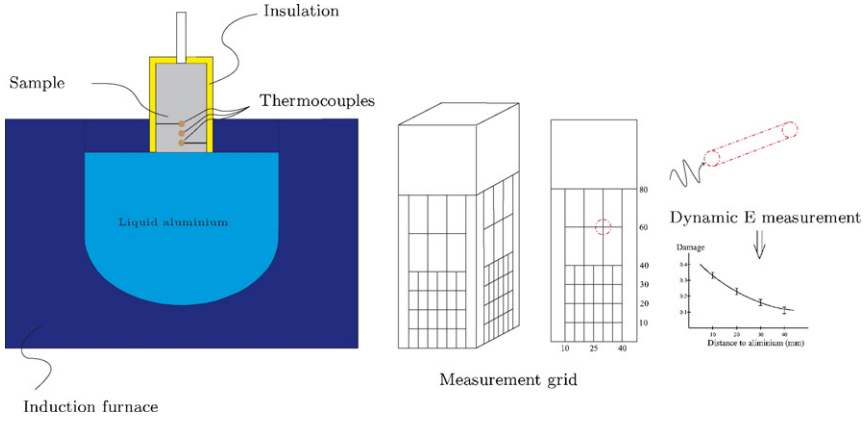


Fig. 3. Molten aluminium thermal shock test set-up.

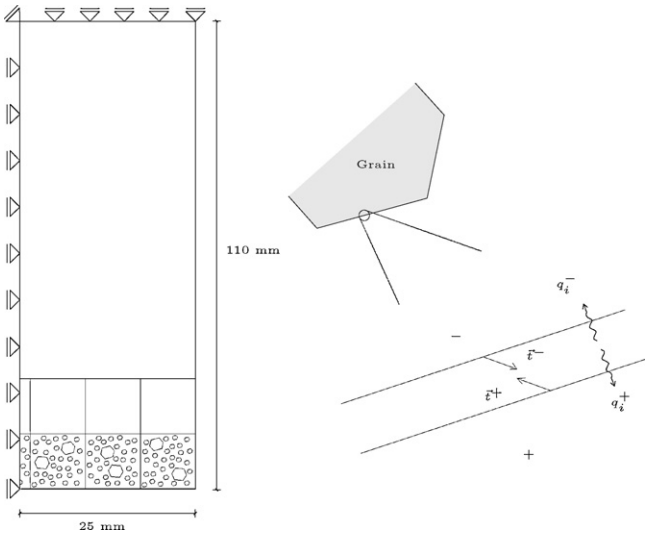


Fig. 4. Direct numerical simulation model and traction and heat flux conditions across a grain–matrix interface

embedded in a matrix of $Al_2O_3$ and mullite which is in fact the sintered, continuous structure of grains smaller than 0.5 μm. Therefore, grains, matrix and their interfaces are the three distinct components which collectively determine the response of the material and have to be addressed in the computational model.

Due to unaffordable computational costs of a 3D model, a fully detailed 2D model of the test sample is constructed as shown in Fig. 4. To this end, volume fractions and basic geometrical information is used to construct, geometrically and physically representative volumetric units of the material. To achieve a geometric randomness in the distribution of the particles, four geometrically different unit volumes and their arbitrarily rotated versions are combined to built-up the full DNS model.

The sample is brought into contact with the molten aluminium reservoir (which is at 1000 °C) for 20 min ('thermal shock phase'). This is followed by a passive 'cooling phase' of 48 h at room temperature (25 °C). The heat transfer characteristics between the sample and the reservoir are identified in Ref. 15 and resulted in temperature dependent heat transfer coefficient according to

$$h = 204.56 + e^{0.0082\theta_f}\ (\mathrm{W/m^2\ K}) \tag{1}$$

where $\theta_f$ is the film temperature defined as $\theta_f = 0.5(\theta_{ambient} + \theta_{surface})$. The same study revealed that the heat loss from the sample during passive cooling takes place at a very slow rate compared to the thermal shock phase and therefore this stage is not really relevant as far as damage initiation and evolution is concerned. Half of the sample is modeled due to symmetry and rigid body motions are properly constrained as shown in Fig. 4. Sides and top surfaces of the sample are thermally insulated which is reflected by imposing heat flux free boundary conditions on these surfaces. The stress/strain state is assumed to satisfy plane strain conditions, which is of course an approximation since the real stress state is 3D due to loading conditions and specimen dimensions. The results of a 2D analysis are reliable for a qualitative investigation and they are representative in terms of trends in damage distribution as a function of the model parameters.

A thermo-mechanical analysis is carried out to determine the evolution of stresses, damage and temperature within the domain. Based on the conservation of linear momentum and energy, the quasi-static mechanical equilibrium in terms of Cauchy stresses

$$\vec{\nabla} \cdot \boldsymbol{\sigma} + \vec{b} = \vec{0} \tag{2}$$

and the transient heat conduction equation,

$$\rho c_v \dot{\theta} + \vec{\nabla} \cdot \vec{q} = 0 \tag{3}$$

apply. In here, $\vec{b}$ is the body force vector, $\vec{\nabla}$ is the gradient operator with respect to the current configuration, $c_v$ is the heat capacity, $\rho$ is the density, $\theta$ is temperature and $\vec{q}$ is the heat flux vector. In addition to external boundary conditions, along the material interfaces between the grains and the matrix, the

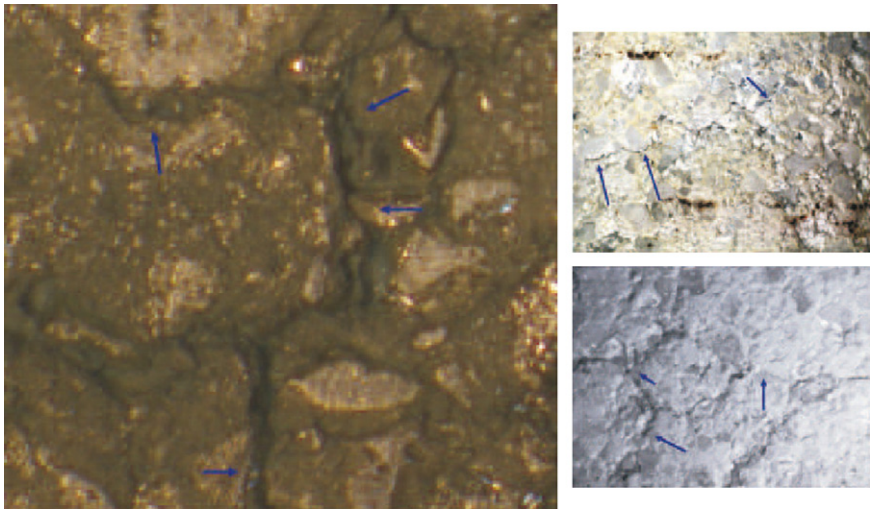

Fig. 5. Microstructure after thermal shock (arrows indicating cracks)

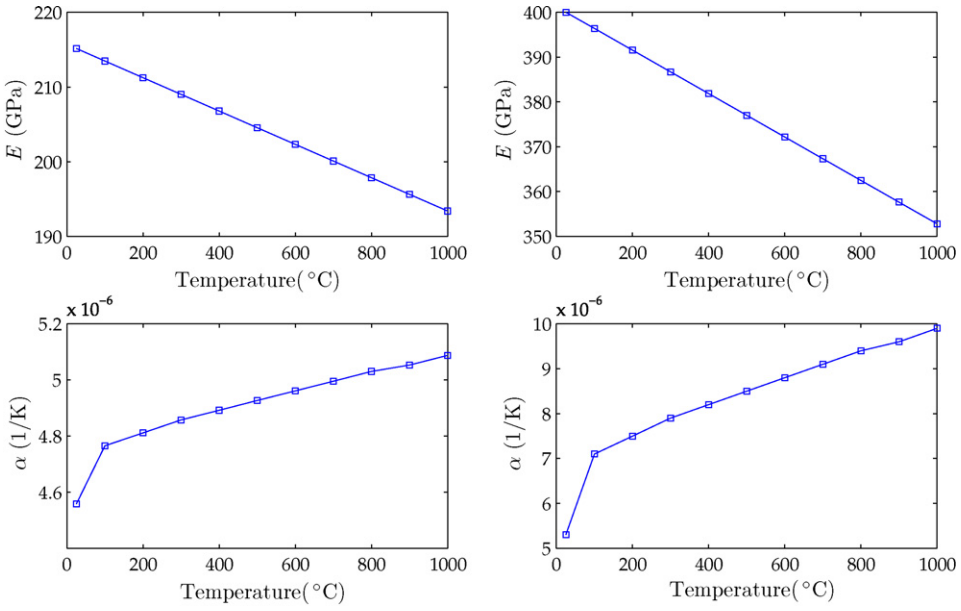


Fig. 6. Temperature dependency of Young's modulus ($E$) and coefficient of thermal expansion ($\alpha$), left column for matrix, right column for grains; based on Refs. 16–19.

conditions,

$$\vec{t}^{+} = -\vec{t}^{-} \quad \text{and} \quad q_i^{+} = -q_i^{-} \tag{4}$$

have to be satisfied, where $\vec{t}$ and $q_i$ are the tractions and interface heat fluxes as shown in Fig. 4. Furthermore subscripts and superscripts + and − indicate that the interface is approached from two different bulk sides of the interface. Solution of these equations requires the constitutive laws for $\boldsymbol{\sigma}$, $\vec{q}$ and in the context of thermo-mechanical cohesive interfaces also for $\vec{t}$ and $q_n$. In the following subsections, the constitutive laws for each phase (grains, matrix and interfaces), are summarized.

### 4.1. Grains

In Fig. 5, microscopic images of thermally shocked samples are shown. As far as large alumina grains are concerned, these images support that micro-cracking occurs along the boundaries of large grains while the grains themselves remain intact. In addition to these experimental investigations, analytical studies on simplified material systems,[5] reveal that above a critical grain size, upon a uniform temperature change, the cracking occurs along matrix–grain interfaces. Therefore the large alumina grains are assumed to behave elastic and not damaging. Based on the data given for 99.5% pure alumina technical ceramics, the Young's modulus is taken to be 400 GPa with the corresponding temperature dependency as shown in Fig. 6. The same reference suggests a temperature independent value of 0.28 for Poisson's ratio. Similarly, temperature dependent conductivity, heat capacity and CTE of the grains are given in Fig. 7, based on the data given in Refs. 16–19. A linear relation between the Cauchy stresses and logarithmic strains is adopted and heat fluxes are determined by Fourier's law of heat conduction.

### 4.2. Matrix

The failure within the matrix takes place through a distributed micro-cracking mechanism. In spite of remarkable achievements in the modeling of discontinuities by novel discretization techniques (X-FEM, generalized FEM), the resolution of complex micro-cracking processes such as multiple micro-cracking and crack bridging cannot be tackled trivially with the aid of these tools. Therefore the failure of matrix phase is handled in an average sense by using a continuum damage mechanics (CDM) approach.

The volumetric percentages of mullite, alumina and porosity within the matrix are 74.48%, 11.52% and 14%, respectively. Mechanical and thermo-physical properties of the matrix are determined by the rule of mixtures, whereby the percentages of alumina and porosity are low in the matrix mixture. The resulting properties and their temperature dependencies are given in Figs. 6 and 7.

As micro-cracks nucleate and propagate within the matrix phase, the coherent structure disintegrates and the stiffness of the matrix decreases. Continuum damage mechanics provides a versatile and computationally feasible framework to model the failure process in an average sense, in a continuum setting without resolving the discontinuities explicitly. The isotropic damage ($D$) is introduced as a field variable, which governs (determines) the current material stiffness as,

$$\mathbb{E} = (1 - D)\mathbb{E}_0 \tag{5}$$

where $\mathbb{E}$ is the current stiffness tensor. The evolution of damage represents the onset or 'nucleation' of micro-cracks and the material gradually loses its stiffness until a complete crack is formed at $D = 1$. The propagation is governed by the local

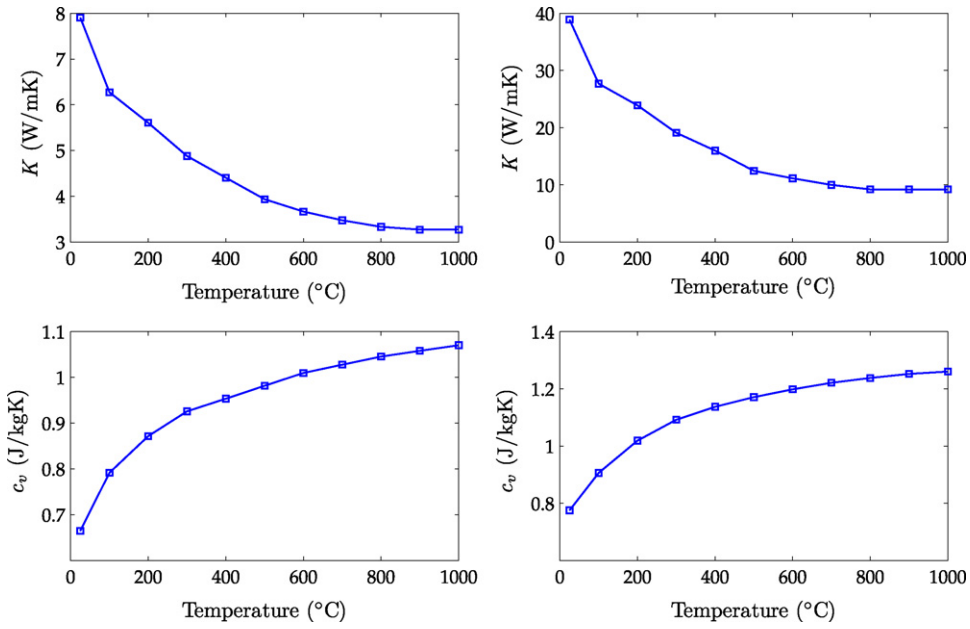


Fig. 7. Temperature dependency of conductivity ($K$) and heat capacity ($c_v$), left column for matrix, right column for grains; based on Refs. 19–22.

stress/strain distribution within the close vicinity of the process zone.

It can be shown easily that damage models based on a classical local continuum description yield results that are dependent on the spatial discretization. More precisely, the results converge to a non-physical solution upon mesh refinement, while less and less energy (zero in the limit) for crack propagation is required. By introducing non-locality in the damage law, either through spatial averaging or through gradient terms, these non-physical results are avoided.

In here, the damage evolution is expressed as a function of a non-local equivalent strain and the damage increases as soon as the non-local equivalent strain level surpasses the maximum non-local equivalent strain value attained during loading history. In an implicit gradient formulation,[23] non-local equivalent strain, $\bar{\epsilon}$, which governs the evolution of damage, is determined through the solution of the Helmholtz equation,

$$\bar{\epsilon} - l^2\nabla^2\bar{\epsilon} = \tilde{\epsilon} \tag{6}$$

which is driven by the local equivalent strain $\tilde{\epsilon}$ in the right-hand side. In Eq. (6), $\nabla^2$ is the nabla operator and $l$ is the internal length scale. Since the non-local strain is not given explicitly in terms of $\tilde{\epsilon}$ and its derivatives, but obtained through the solution of Eq. (6) over the domain, the resulting formulation is referred to as the implicit gradient formulation distinguishing it from explicit formulations existing in the literature.

The solution of Eq. (6) requires the definition of proper boundary conditions on the external boundaries and the boundaries between the matrix and the non-damaging grains, which are commonly adopted the natural boundary conditions,

$$\vec{\nabla}\bar{\epsilon}\cdot\vec{n} = 0 \tag{7}$$

Based on Ref. 24, the equivalent local strain is defined as,

$$\tilde{\epsilon} = \frac{k-1}{2k(1-2\nu)}I_1 + \frac{1}{2k}\sqrt{\frac{(k-1)^2}{(1-2\nu)^2}I_1^2 - \frac{12k}{(1+\nu)^2}J_2} \tag{8}$$

where $I_1$ and $J_2$ are the first invariant of the strain tensor and second invariant of the deviatoric strain tensor, respectively. Under uni-axial loading conditions, the equivalent local strain is defined such that, a compressive stress of $k\sigma$ leads to the same damage growth as a tensile stress of $\sigma$. The characteristic large ratio of compressive strength vs. tensile strength of quasi-brittle materials is incorporated by the variable $k = (f_c/f_t)$. The particular damage law used here has the form,

$$D = \begin{cases} 0 & \text{if } \kappa < \kappa_0 \\ \left(\dfrac{\kappa-\kappa_0}{\kappa_f-\kappa_0}\right)^{\gamma} & \text{if } \kappa > \kappa_0 \\ 1 & \text{if } \kappa > \kappa_f \end{cases}$$

which is complemented with the conventional loading/unloading conditions,

$$\dot{\kappa} \geq 0, \quad \bar{\epsilon} - \kappa \leq 0, \quad \dot{\kappa}(\bar{\epsilon} - \kappa) = 0 \tag{9}$$

$\kappa_0$ denotes the damage initiation threshold and $\kappa_f$ is the upper bound leading to a critical damage equalling unity. A constant-$\tilde{\epsilon}$ curve and the damage evolution law are shown in Fig. 8. As the Poisson's ratio ($\nu$) approaches to 0.5 and/or under strongly deviatoric strain states, special care has to be taken since the expression within the square root might become undefined or negative.

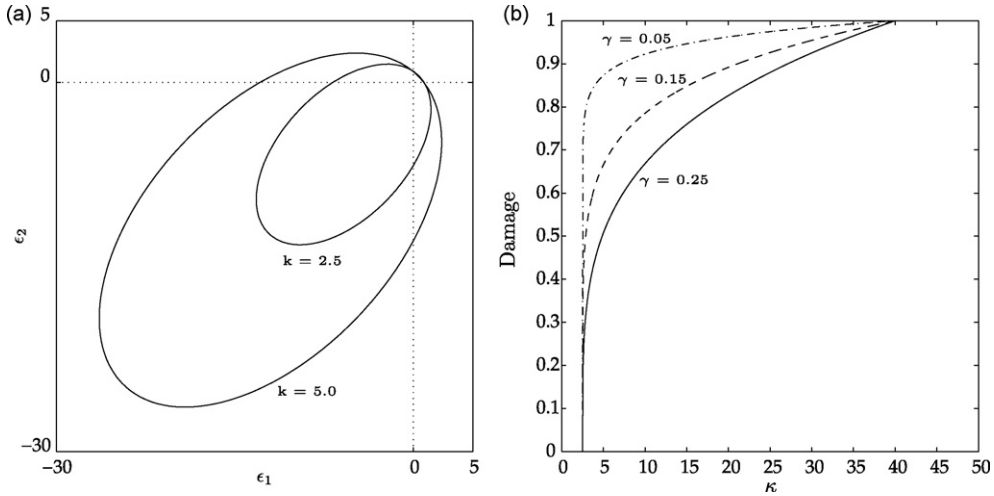


Fig. 8. (a) Equivalent local strain definition in principal strain space (for $\tilde{\epsilon} = 1.5$, $\mu = 0.2$, plane strain conditions) and (b) damage evolution law.

### 4.3. Interfaces

Since the mechanical behaviour and heat transfer mechanisms heavily depend on the status of the interfaces, the modeling and characterization of the interfaces are crucial. Refractory materials exhibit a quasi-brittle response upon mechanical loading which indicates that the micro-cracking mechanisms have a cohesive nature due to crack bridging mechanisms, connecting the surfaces of newly forming micro-cracks. Therefore, the interfaces between the grains and the matrix are modeled as thermo-mechanical cohesive zones where the load and heat transfer mechanisms weaken as the opening between the two faces of the newly forming crack (crack increment) increases. Direct experimental characterization of the interfaces still remains a challenging task for the experimentalists since it is intrinsically difficult to develop an experimental set-up and suitable samples that enable reliable measurements at such small scales. Therefore, the parameters of the traction-opening laws are determined inversely by using the thermal shock test results.

The cohesive nature of interfaces are described by the well-established mechanical interface relations through which the damage at the micro-crack tip is lumped into traction-opening relations. These relations are typically characterized by the shape of the response curve, fracture energy and the peak traction values. As reported in Ref. 25, the decisive parameters are the fracture energy and the strength of the interface rather than the particular formulation of the traction-opening law. Therefore, in this paper, normal and tangential tractions are described by the smooth expressions (improved Xu–Needleman traction–opening laws, see Ref. 26),

$$t_n = \frac{\phi_n}{\delta_n}\left(\frac{\Delta_n}{\delta_n}\right)\exp\left(-\frac{\Delta_n}{\delta_n}\right)\exp\left(-\frac{\Delta_t^2}{\delta_t^2}\right) \tag{10a}$$

$$t_t = 2\frac{\phi_t}{\delta_t}\left(\frac{\Delta_t}{\delta_t}\right)\left(1+\frac{\Delta_n}{\delta_n}\right)\exp\left(-\frac{\Delta_t^2}{\delta_t^2}\right)\exp\left(-\frac{\Delta_n}{\delta_n}\right) \tag{10b}$$

where $\phi_n$ and $\phi_t$ are the fracture energies in pure opening and pure sliding modes, respectively.[26] $\delta_n$ and $\delta_t$ are the mechanical openings in normal and tangential directions as shown in Fig. 9, in a finite element discretization setting. For a consistent description of unloading–reloading, a damage parameter based on the definition of an effective opening measure,

$$\Delta_{eff} = \sqrt{\Delta_n^2 + \beta^2\Delta_t^2} \quad \text{with} \quad \beta = 0.5 \tag{11}$$

is introduced and the maximum effective opening attained is traced at every integration point of the interface element. Loading takes place when $\Delta_{eff} = \Delta_{max}$ and $\dot{\Delta}_{eff} \geq 0$ and unloading (or reloading) when $\Delta_{eff} < \Delta_{max}$. In the context of thermo-mechanical loading, the heat conduction through the interfaces will decrease as well if the opening increases. In fact, the heat transfer through the solid phase is obstructed and the air filling the crack will act as a substitute secondary conducting medium for the heat flow between the two faces of the crack. To quantify the heat flow along the interfaces on the basis of physical mechanisms, the mechanical interface description is supplemented

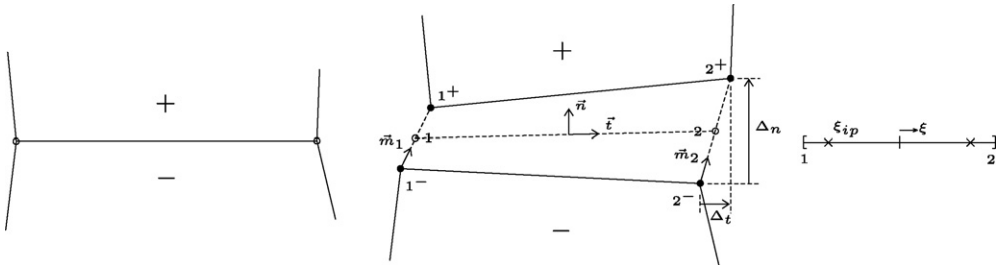


Fig. 9. Two-noded interface element, undeformed and deformed configurations.

with a thermal interface element description as presented in Ref. 27 where the heat flux through the interface is defined as,

$$q_i = \sqrt{q_n^2 + q_t^2} \tag{12}$$

with the components

$$q_n = ((1-d)k_s + k_g)[\![\theta]\!]\vec{m}\cdot\vec{n} \tag{13a}$$

$$q_t = (1-d)k_s[\![\theta]\!]\vec{m}\cdot\vec{t} \tag{13b}$$

to be determined at each integration point based on the interpolation

$$[\![\vec{\theta}]\!] = N_1(\theta_{1^+} - \theta_{1^-})\vec{m}_1 + N_2(\theta_{2^+} - \theta_{2^-})\vec{m}_2 \quad \text{with}$$
$$\vec{m}_1 = \frac{\vec{x}_{1^+} - \vec{x}_{1^-}}{||\vec{x}_{1^+} - \vec{x}_{1^-}||} \text{ and } \vec{m}_2 = \frac{\vec{x}_{2^+} - \vec{x}_{2^-}}{||\vec{x}_{2^+} - \vec{x}_{2^-}||} \tag{14}$$

$[\![\theta]\!]$ is the temperature difference between two material points on opposite faces of the discontinuity which were coincident before the crack separated them, see Fig. 9. $k^s$ and $k^g$ are the conductance of the interface due to solid crack bridging mechanisms and the gas filling the cavity, respectively. The interface conductance can be considered as a penalty parameter which enforces an identical temperature value at both sides in the case of an undamaged interface. The interfacial damage parameter $d$ of Eq. (12) is defined as the ratio $(\Delta_{eff}^{max}/\Delta_{crt})$ where

$$\Delta_{crt} = \sqrt{\Delta_n^2|_{0.1t_n^{max}} + \beta^2\Delta_t^2|_{0.1t_t^{max}}} \tag{15}$$

and $\Delta_{n,t}|_{0.1t_{n,t}^{max}}$ corresponds to the normal and tangential openings corresponding to the residual values $0.1t_n^{max}$ and $0.1t_t^{max}$ in the post-peak regime of the traction-opening curves, respectively. In case of crack closure, the contact conductance is mainly governed by the ratio of the actual contact area to the total interface area. A contact damage variable representing this ratio can be used in the case of crack closure as,

$$q_{n,c} = -((1-d_c)k_s)[\![\theta]\!]\vec{m}\cdot\vec{n} \tag{16a}$$

$$q_{t,c} = 0 \tag{16b}$$

Since the fraction of crack bridges are expected to be dominant in crack closure as well, one can assume that $d_c \approx d$, as long as full separation did not occur.

### 4.4. Solution procedure

In addition to the quasi-static equilibrium and the heat balance, the non-locality (Helmholtz) equation has to be fulfilled at every material point of the matrix. The quasi-static equilibrium equation and the Helmholtz equation are coupled through the direct dependence of stresses on the damage field and the dependence of damage values on the non-local equivalent strains.

An incremental-iterative solution procedure within a finite element framework, is adopted to solve the three coupled field equations. Here, instead of solving the coupled equations in a combined way, the global problem is split-up into three incrementally uncoupled problems

$$\int_V \vec{q}\cdot\vec{\nabla}\delta\theta\,dV = \int_{\Gamma_q}\bar{q}\delta\theta\,d\Gamma + \int_{\Gamma_i} q_n|_+(\delta\theta^+ - \delta\theta^-)\,d\Gamma \tag{17a}$$

$$\int_V \sigma : \vec{\nabla}\delta\vec{u}\,dV = \int_V \vec{b}\cdot\delta\vec{u}\,dV + \int_{\Gamma_t}\vec{\bar{t}}\cdot\delta\vec{u}\,d\Gamma + \int_{\Gamma_i}\vec{t}|_+\cdot(\delta\vec{u}^+ - \delta\vec{u}^-)\,d\Gamma \tag{17b}$$

$$\int_{V_m}\bar{\epsilon}\delta\bar{\epsilon}\,dV - \int_{V_m} l^2\vec{\nabla}\bar{\epsilon}\cdot\vec{\nabla}\delta\bar{\epsilon}\,dV = \int_{V_m}\tilde{\epsilon}\delta\bar{\epsilon}\,dV \tag{17c}$$

where $\Gamma_{\bar{q}}$ and $\Gamma_{\bar{t}}$ are the parts of external boundaries where the heat fluxes and the tractions are prescribed, respectively. $\Gamma_i$ is the area of the grain–matrix interfaces and $V_m$ is the matrix volume. These equations are solved sequentially within a time increment. Therefore, on a mechanically frozen state, the heat conduction equation is solved and the temperature profile is updated accordingly. Thereafter, the stress analysis is carried out with the updated temperature values but assuming a frozen damage state. Finally, the Helmholtz equation is solved with the equivalent strain values which are the driving force for the evolution of non-local equivalent strains. Typical increment of the resulting algorithm is summarized in Table 2. The outlined solution procedure, has been successfully used in the context of numerical damage-plasticity simulations.[28,29] The main disadvantage of the above operator-split solution procedure is its conditional stability which requires sufficiently small time steps. However, as soon as non-linearities are triggered, the incremental-iterative

Table 2
Staggered solution scheme for the thermo-mechanically induced damage analysis

Next increment

**I.** Thermal pass:
**(a)** Next iteration
- assemble the tangent conductivity
- solve the system and update $\theta$
- loop over all integration points and calculate heat flux and tangent conductivity
- assemble the internal nodal fluxes
- check for convergence, if not repeat step (a), else continue

**II.** Mechanical pass:
**(b)** Next iteration
- assemble the tangent stiffness
- solve the system and update $\underline{u}$
- loop over all integration points and calculate stresses and material tangent
- assemble the internal nodal forces
- check for convergence, if not repeat step (b), else continue

**III.** Non-local field pass:
- assemble the system matrices (left-hand side of Eq. (17c)) based on updated geometry
- assemble the right-hand side of Eq. (17c) based on the updated local equivalent strain $\tilde{\epsilon}$
- solve the system, update $\bar{\epsilon}$, $\kappa$ and D
- continue with the next increment

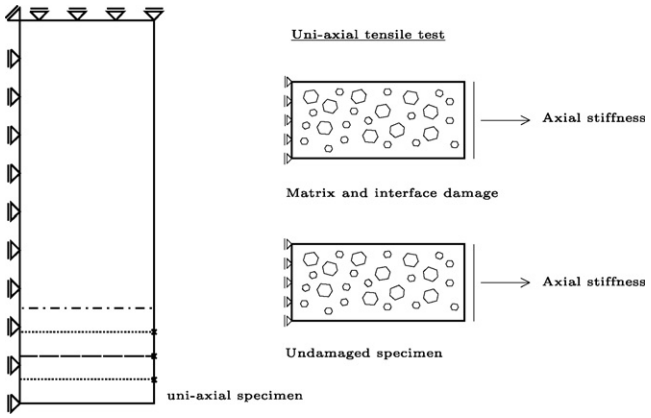


Fig. 10. Equivalent static procedure.

framework requires small time steps in any case. Therefore, the operator-split technique does not substantially increase the real computational costs.

### 4.5. Parameter identification procedure

As concisely mentioned in Section 3, use is made of ultrasonic wave propagation measurements on thermally shocked specimens at various locations along the height as shown in Fig. 3; for a detailed treatment, see Ref. 1. Based on the wave speed measurements, the dynamic Young's modulus is calculated using an inverse method. The same procedure is repeated for undamaged samples and based on the Young's moduli ratio, the damage distribution curve along the height has been determined.

To use the experimental results as a reference to identify the parameters of the numerical model, the following static analysis procedure is pursued. From the computational model (DNS model), subjected to the thermal shock history, uni-axial 'specimens' are cut out at the locations corresponding to the positions of the transducers used for the measurements. The cross-section of the uni-axial specimens is determined by the size of the transducer. The damage and interface opening histories are transferred to these uni-axial specimens.

After extraction of these specimens, they are exposed to uni-axial tensile loading, from which the axial static stiffness of the damaged specimen is determined and compared with the axial stiffness of the corresponding undamaged specimen, see Fig. 10.

Following this procedure, the damage evolution law and interface parameters (see Table 3) are tuned towards the computational results presented in Fig. 11(a). Internal length scale of the matrix damage model is taken as 0.4 mm based on the edge length of the small grains which is linked to the stress ligaments developing between the grains. Preliminary computations indicated that the damage values at locations far from the thermally shocked end of the specimen are essentially determined by the matrix damage parameters $\kappa_0$ and $\kappa_f$. These values are taken as $0.08 \times 10^{-5}$ and $0.09 \times 10^{-2}$ which yielded good agreement with the experimental results.

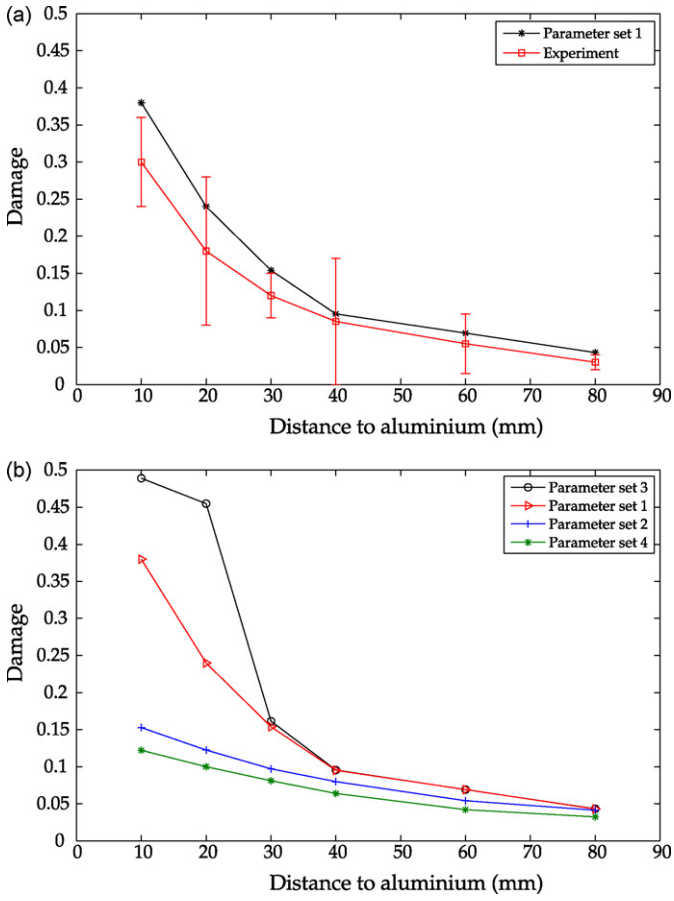


Fig. 11. (a) Damage distribution along the height, experimental vs. computed results and (b) damage distribution with different interface parameters.

Computational results capture the experimentally observed trends well whereas quantitatively the results are over estimating the damage distribution particularly in the close neighborhood of the thermally shocked end of the sample. In this context, it is important to re-emphasize the fact that the experimental measurements result in dynamic Young's modulus whereas the computational results are static values. Typically, the dynamic modulus tends to be smaller than the one estimated from the static modulus,[1] as done in the model.

It is important to note that the computational results could have been reproduced by using a different set of parameters. In other words, the identified parameters are non-unique essentially due to the lack of experimental data.

### 4.6. Parametric study

To investigate the influence of different material parameters, a parametric study is carried out which uses the equivalent static procedure as the basis for damage quantification.

Fully resolved models are particularly powerful in capturing the direct influence of parameters which are difficult to incorporate into equivalent homogenous continuum models. In this context, first the mechanical strength of the interfaces is considered. In Fig. 11(b), computational results with 4 different parameter sets are presented. The model without mechani-

Table 3
Model parameters used for different cases.

| | Set 1 | Set 2 | Set3 | Set4 | Set 5 |
|---|---|---|---|---|---|
| $\phi_n$(J/m$^2$) | 25 | 25 | 25 | – | 25 |
| $\phi_t$(J/m$^2$) | 50 | 50 | 50 | – | 50 |
| $t_n^{max}$(MPa) | 42 | 14 | 56 | – | 700 |
| $t_t^{max}$(MPa) | 84 | 28 | 112 | – | 1400 |
| $\kappa_0$ | $0.08 \times 10^{-5}$ | $0.08 \times 10^{-5}$ | $0.08 \times 10^{-5}$ | $0.08 \times 10^{-5}$ | $0.08 \times 10^{-5}$ |
| $\kappa_f$ | $0.09 \times 10^{-2}$ | $0.09 \times 10^{-2}$ | $0.09 \times 10^{-2}$ | $0.09 \times 10^{-2}$ | $0.09 \times 10^{-2}$ |
| $\gamma$ | 0.95 | 0.95 | 0.95 | 0.95 | 0.95 |
| $l$(mm) | 0.4 | 0.4 | 0.4 | 0.4 | 0.4 |

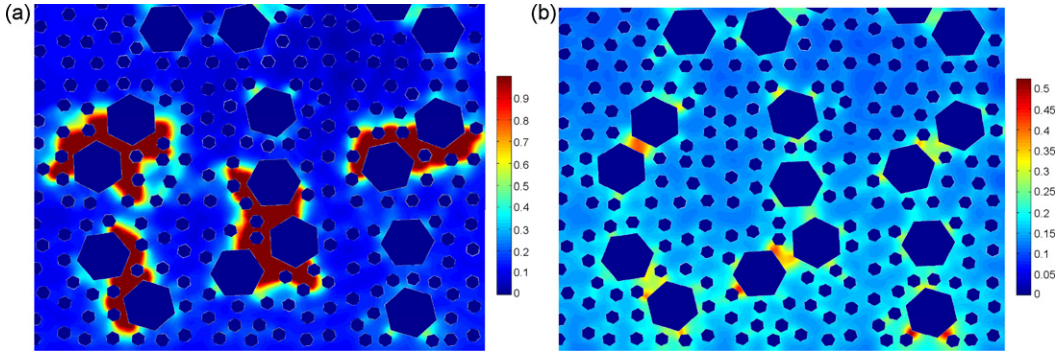


Fig. 12. Damage distribution at the bottom strip of the sample: (a) based on parameter set 1 and (b) based on parameter set 2.

cal interfaces (fully bonded) yields the lower bound solution (parameter set 4, see Table 3), as seen from the figure. The damage values in the close vicinity of the thermally shocked end are increasing as the strength of the interfaces increases with the same fracture energies (more brittle interface). The resulting damage distribution for the bottom strip is shown in Fig. 12 for two different cases. As seen from the figure, islands of fully damaged zones are formed for higher strength values.

In fact, the damage is initiated in the compression regions between the grains. As the interface becomes more brittle, especially the tangential openings (sliding) of the interfaces located on the faces of larger grains get larger (compared to the more ductile case) whereby the grains tend to rotate due to geometric lay-out. It means that the compressive action between the grains and the matrix becomes pronounced, leading to high damage values. The damage spreads to a certain area as the compressive region evolve as the matrix damages. Accordingly, as the traction strengths are further increased as done with parameter set 5, the failure pattern disappears, see Fig. 13, as the tangential opening values become very small since almost all of the interfaces remain within the pre-peak, stiff regime of the traction-opening relations. In the limit, the pattern should approach to the case where there are no interfaces in the system (i.e. fully bonded), which is presented in Fig. 13. Motivated by the 'short range' and 'long range' effects introduced in Section 1, the influence of the CTE mismatch between the grains and the matrix ('short range' effect) is investigated next. As shown in Fig. 14(a), in case of identical CTE's (see Table 5), damage values are much smaller than in the reference case. On the other hand, a slight increase in the CTE mismatch yields a considerable difference in the resulting damage profile, which indicates a strong sensitivity.

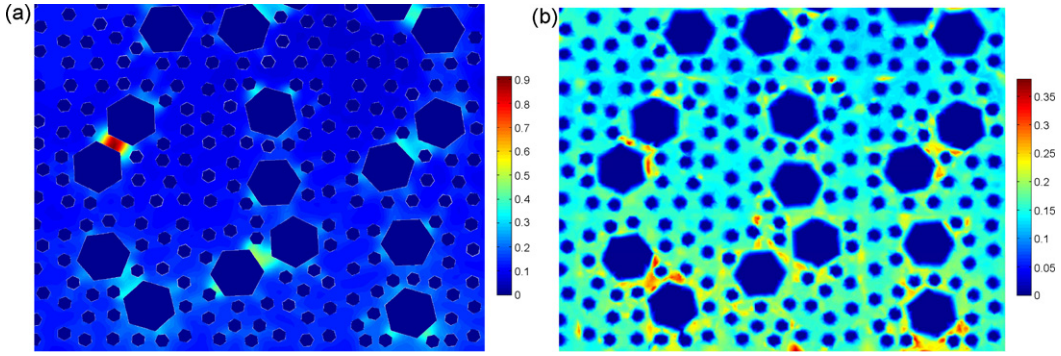


Fig. 13. Damage distribution at the bottom strip of the sample: (a) based on parameter set 5 and (b) based on parameter set 4 (without interfaces).

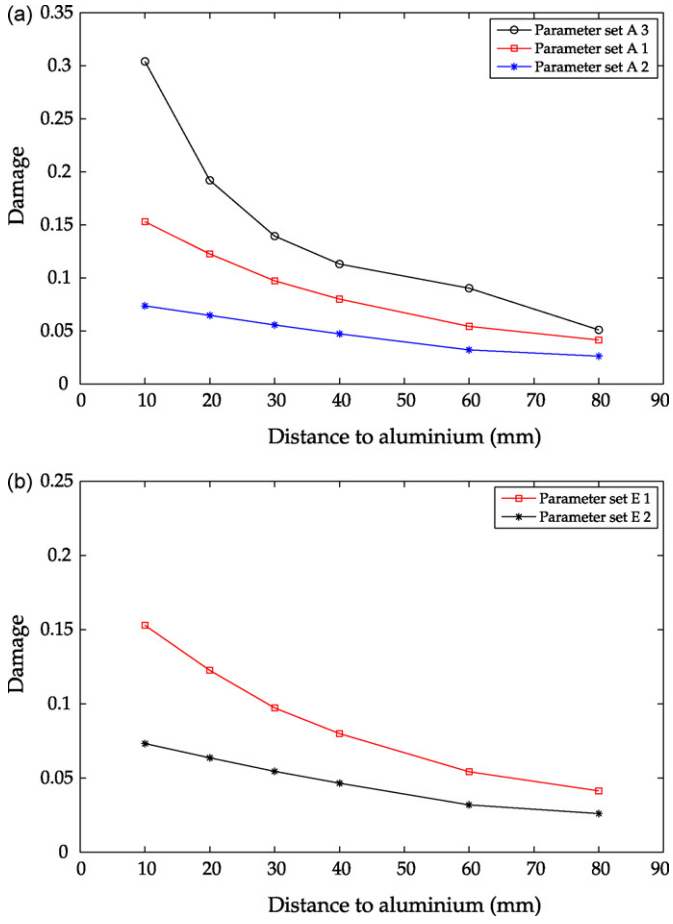


Fig. 14. (a) Damage distribution as a function of CTE mismatch and (b) damage distribution as a function of matrix stiffness.

In Fig. 14(b), the damage values obtained by increasing the matrix stiffness are compared with the reference solution (parameter set $E$ 1 and $E$ 2, Table 4). A more stiff matrix results in reduced damage values throughout the specimen.

The 'long range' effect is associated with the temperature gradient which is determined by the diffusivity of the material and the heat transfer conditions across the boundaries. To investigate this effect, the conductivities of the both phases have been increased significantly as reported in Table 5 (parameter set $K$ 1 and $K$ 2). The resulting temperature profile along the indicated section for two cases are shown in Fig. 15. In case of higher conductivities, the temperature difference between the top and bottom faces of the specimen gets considerably smaller compared to the reference case, which also implies a deformation mode closer to a homogenous state. The resulting damage values are shown in Fig. 16. This result suggests that as the temperature profile gets milder, the damage values tend to be smaller and approximately constant throughout the specimen. To investigate the influence of interfaces when the material is highly conductive, another set of computations is carried out as given in Table 5 (parameter set $K$ 3). The results given in Fig. 16(b) suggests that as the material gets more conductive, the influence of interface parameters become negligible since the two data sets are almost coincident. As the deformation approaches to a homogenous state, the interfacial characteristics become less influential.

Table 4
Model parameters used for different cases (room temperature values).

| | $E$ 1 | $E$ 2 |
|---|---|---|
| $\phi_n$(J/m$^2$) | 25 | 25 |
| $\phi_t$(J/m$^2$) | 50 | 50 |
| $t_n^{max}$(MPa) | 14 | 14 |
| $t_t^{max}$(MPa) | 28 | 28 |
| $\kappa_0$ | $0.08 \times 10^{-5}$ | $0.08 \times 10^{-5}$ |
| $\kappa_f$ | $0.09 \times 10^{-2}$ | $0.09 \times 10^{-2}$ |
| $\gamma$ | 0.95 | 0.95 |
| $l$(mm) | 0.4 | 0.4 |
| $K_m$(W/m$^2$ K) | 7.91 | 7.91 |
| $K_g$(W/m$^2$ K) | 38.90 | 38.90 |
| $E_m$(GPa) | 215.14 | 322.71 |
| $E_g$(GPa) | 400 | 400 |
| $\alpha_m$(1/K) | $4.56 \times 10^{-6}$ | $4.56 \times 10^{-6}$ |
| $\alpha_g$(1/K) | $5.3 \times 10^{-6}$ | $5.3 \times 10^{-6}$ |

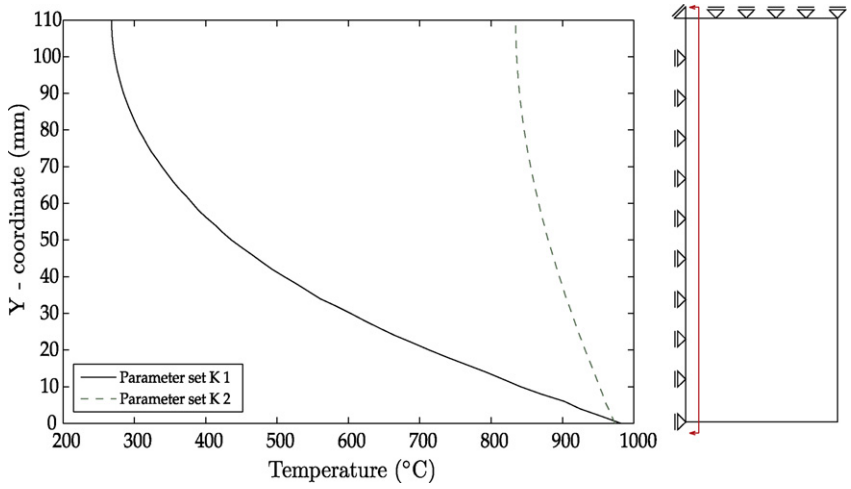


Fig. 15. Temperature profile at the end of loading history for parameter set $K$ 1 and $K$ 2.

Table 5
Model parameters used for different cases (room temperature values).

| | $A\,1$ | $A\,2$ | $A\,3$ | $K\,1$ | $K\,2$ | $K\,3$ |
|---|---|---|---|---|---|---|
| $\phi_n$(J/m$^2$) | 25 | 25 | 25 | 25 | 25 | 25 |
| $\phi_t$(J/m$^2$) | 50 | 50 | 50 | 50 | 50 | 50 |
| $t_n^{max}$(MPa) | 14 | 14 | 14 | 14 | 14 | 56 |
| $t_t^{max}$(MPa) | 28 | 28 | 28 | 28 | 28 | 112 |
| $\kappa_0$ | $0.08 \times 10^{-5}$ | $0.08 \times 10^{-5}$ | $0.08 \times 10^{-5}$ | $0.08 \times 10^{-5}$ | $0.08 \times 10^{-5}$ | $0.08 \times 10^{-5}$ |
| $\kappa_f$ | $0.09 \times 10^{-2}$ | $0.09 \times 10^{-2}$ | $0.09 \times 10^{-2}$ | $0.09 \times 10^{-2}$ | $0.09 \times 10^{-2}$ | $0.09 \times 10^{-2}$ |
| $\gamma$ | 0.95 | 0.95 | 0.95 | 0.95 | 0.95 | 0.95 |
| $l$(mm) | 0.4 | 0.4 | 0.4 | 0.4 | 0.4 | 0.4 |
| $K_m$(W/m$^2$ K) | 7.91 | 7.91 | 7.91 | 7.91 | 79.1 | 79.1 |
| $K_g$(W/m$^2$ K) | 38.90 | 38.90 | 38.90 | 38.90 | 389.0 | 389.0 |
| $E_m$(GPa) | 215.14 | 215.14 | 215.14 | 215.14 | 215.14 | 215.14 |
| $E_g$(GPa) | 400 | 400 | 400 | 400 | 400 | 400 |
| $\alpha_m$(1/K) | $4.56 \times 10^{-6}$ | $4.56 \times 10^{-6}$ | $4.56 \times 10^{-6}$ | $4.56 \times 10^{-6}$ | $4.56 \times 10^{-6}$ | $4.56 \times 10^{-6}$ |
| $\alpha_g$(1/K) | $5.3 \times 10^{-6}$ | $4.56 \times 10^{-6}$ | $5.472 \times 10^{-6}$ | $5.3 \times 10^{-6}$ | $5.3 \times 10^{-6}$ | $5.3 \times 10^{-6}$ |

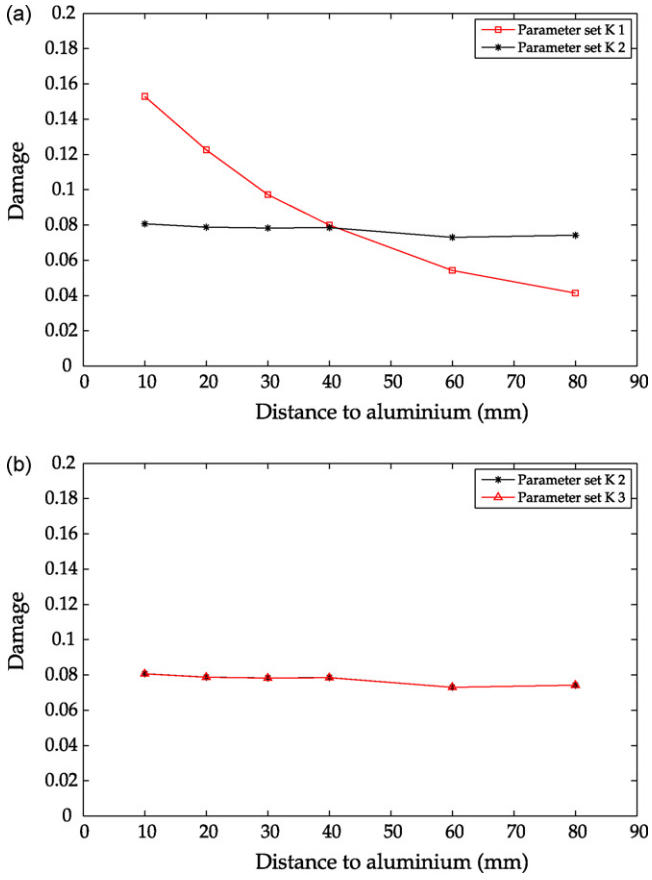


Fig. 16. (a) Damage distribution for a more conductive material and (b) influence of the interface strength in case of more conductive material.

## 5. Summary and conclusion

On the basis of an idealized two-phase material system, direct numerical simulations are used to investigate the thermal shock response of refractory ceramics. Molten aluminium tests are reproduced within a computational framework and the parameters of the model are identified relying on a static equivalent computational procedure. Furthermore the influence of certain material parameters are investigated qualitatively.

On the basis of this parametric study, it can be concluded that:

- In case of strong temperature gradients, the damage evolution is markedly sensitive to the CTE mismatch between the phases. Damage values increase significantly as a result of a slight change in the contrast between the CTE of the phases.
- The brittleness of the interfaces has a strong influence as long as there exists a strong temperature gradient. More brittle interfaces (with a limited strength) yield higher damage values. However, as the temperature profile gets milder, the influence of the mechanical characteristics of the interfaces become less significant.
- For highly conductive materials, the damage distribution tends to be uniform throughout the specimen. The influence of interface parameters diminishes since the deformation mode is approaching a homogenous state and the damage values are smaller since the CTE mismatch is the only mechanism of the damage evolution.
- Increasing the stiffness of the matrix has a favorable effect in the context of thermal shock response since the damage values are getting smaller.

Obviously, a more extensive parametric study can be carried out to investigate the relations between different parameters. Nevertheless, the modeling approach and the parametric study provides information on the mechanisms of damage evolution and the significance of certain parameters of the material system of interest. Such information can not be extracted on the basis of a continuum model which does not consider the heterogeneities explicitly. Furthermore, the identified parameters can be useful in a multi-scale modeling framework.

## References

1. Damhof F, Brekelmans WAM, Geers MGD. Experimental analysis of the evolution of thermal shock damage using transit time measurement of ultrasonic waves. *Journal of the European Ceramics Society* 2009 [available online].
2. Hasselman DPH. Strength behaviour of polycrystalline alumina subjected to thermal shock. *Journal of the American Ceramic Society* 1970;**53**(9):490–5.

3. Gupta TK. Strength degradation and crack propagation in thermally shocked $Al_2O_3$. *Journal of the American Ceramic Society* 1971;**55**(5):249–53.
4. Ziegler G. Microstructural aspects of thermal stress resistance of high-strength engineering ceramics—Part I. *Zeitschrift für Werkstofftechnik* 1985;**16**:12–8.
5. Evans AG, Fu Y. Some effects of microcrack on the mechanical properties of brittle solids. I. Stress, strain relations. *Acta Metallurgica* 1985;**33**:1515–23.
6. Tvergaard V, Hutchinson WJ. Microcracking in ceramics induced by thermal expansion or elastic anisotropy. *Journal of the American Ceramic Society* 1988;**71**(3):157–66.
7. Laws N, Lee JC. Microcracking in polycrystalline ceramics: elastic isotropy and thermal anisotropy. *Journal of the Mechanics and Physics of Solids* 1989;**37**(5):603–18.
8. Joliff Y, Absi J, Glandus JC, Huger M, Tossier-Doyen N. Experimental and numerical study of the thermo-mechanical behaviour of refractory model materials. *Journal of the European Ceramic Society* 2007;**27**: 1513–20.
9. Andreev K, Harmuth H. FEM simulation of the thermo-mechanical behaviour and failure of refractories—a case study. *Journal of the Materials Processing Technology* 2003;**143–144**:72–7.
10. Gawin D, Pesavento F, Schrefler BA. Simulation of damage-permeability coupling in hygro-thermo-mechanical analysis of concrete at high temperature. *Communications in Numerical Methods in Engineering* 2002;**18**:113–9.
11. Pearce CJ, Nielsen CV, Bicanic N. Gradient enhanced thermo-mechanical damage model for concrete at high temperatures including transient thermal creep. *International Journal for Numerical and Analytical Methods in Geomechanics* 2004;**28**:715–35.
12. Damhof F, Brekelmans WAM, Geers MGD. Non-local modeling of thermal shock damage in refractory materials. *Engineering Fracture Mechanics* 2008;**75**:4706–20.
13. Özdemir I, Brekelmans WAM, Geers MGD. $FE^2$ computational homogenization for the thermo-mechanical analysis of heterogeneous solids. *Computer Methods in Applied Mechanics and Engineering* 2008;**198**:602–13.
14. Gorter, H., Franken, M., Sinema, S., Boersma, J. and Damhof, E. Betere Temperatuurwissel Bestendigheid (BTW) Eindrapport (in Dutch). Netherlands Organisation for Applied Scientific Research Report; 2008.
15. Damhof F, Tesselaar W, Van den Eynden JC. A novel experimental approach to investigate thermal shock damage in refractory materials. *Ceramic Forum International* 2007;**84**:75–9.
16. Kumazawa T, Ohta S, Kanzaki S, Sakaguchi S, Tabata H. Elastic properties of mullite ceramics at elevated temperature. *Journal of Materials Science Letters* 1989;**8**:47–8.
17. Ledbetter H, Kim S, Balzar D. Elastic properties of mullite. *Journal of the American Ceramic Society* 1998;**81**(4):1025–8.
18. Schreuer J, Hildmann B, Schneider H. Elastic properties of mullite single crystals up to 1400 C. *Journal of the American Ceramic Society* 2006;**89**(5):1624–31.
19. Morrel R. *Handbook of properties of technical and engineering ceramics*. HSMO Publications; 1987.
20. Barea R, Osendi MI, Ferreira JMF, Miranzo P. Thermal conductivity of highly porous mullite material. *Acta Materialia* 2005;**53**:3313–8.
21. Schneider H, Schreuer J, Hildmann B. Structure and properties of mullite—a review. *Journal of the European Ceramic Society* 2008;**28**:329–44.
22. Hildmann B, Schneider H. Heat capacity of mullite: new data and evidence for a high-temperature phase transformation. *Journal of the American Ceramic Society* 2004;**87**(2):227–34.
23. Peerlings, R. H. J. Enhanced Damage Modelling for Fracture and Fatigue. Ph.D. Thesis. Eindhoven University of Technology; 1999.
24. de Vree JHP, Brekelmans WAM, van Gils MAJ. Comparison of nonlocal approaches in continuum damage mechanics. *Computers and Structures* 1995;**55**:581–8.
25. Chandra N, Li H, Shet C, Ghonem H. Some issues in the application of cohesive zone models for metal–ceramic interfaces. *International Journal of Solids and Structures* 2002;**39**:2827–55.
26. van den Bosch MJ, Schreurs PJG, Geers MGD. An improved description of the exponential Xu and Needleman cohesive zone law for mixed-mode decohesion. *Engineering Fracture Mechanics* 2006;**73**(9):1220–34.
27. Özdemir, I., Brekelmans, W. A. M. and Geers, M. G. D. A thermo-mechanical cohesive zone model; submitted for publication.
28. Boers SHA, Schreurs PJG, Geers MGD. Operator-split damage-plasticity applied to groove forming in food can lids. *International Journal of Solids and Structures* 2005;**42**(14):4154–78.
29. Mediavilla J, Peerlings RHJ, Geers MGD. An integrated continuous–discontinuous approach towards damage engineering in sheet metal forming processes. *Engineering Fracture Mechanics* 2006;**73**(7):895–916.